Journal of Power Sources 679 (2026) 240246

Contents lists available at ScienceDirect

Journal of Power Sources

journal homepage: www.elsevier.com/locate/jpowsour

Operando and *in situ* insights into cobalt selenide cathodes for rechargeable aluminum batteries: Conversion mechanism, degradation pathways and electrolyte interactions

Eliana Fuentes-Mendoza [a,*], Angelina Sarapulova [a,b,c,d], Ramon Zimmermanns [a], Amirhossein Dorosti [a], Volodymyr Baran [e], Fabian Jeschull [a], Sonia Dsoke [a,b,c,d]

[a] Institute for Applied Materials (IAM), Karlsruhe Institute of Technology (KIT), Hermann-von-Helmholtz-Platz 1, Eggenstein-Leopoldshafen, 76344, Germany
[b] Department of Electrical Energy Storage, Fraunhofer Institute for Solar Energy Systems, Heidenhofstr. 2, Freiburg, 79110, Germany
[c] Freiburg Materials Research Center-FMF, University of Freiburg, Stefan-Meier Str. 21, Freiburg, 79104, Germany
[d] Institute for Sustainable Systems Engineering (INATECH), University of Freiburg, Emmy-Noether-Straße 2, Freiburg, 79110, Germany
[e] Deutsches Elektronen-Synchrotron DESY, Notkestraße 85, Hamburg, 22607, Germany

HIGHLIGHTS

- Capacity originates from reversible Se redox rather than Co.
- Cobalt dissolves and migrates to the anode, triggering capacity fade.
- *Operando* XRD and XAS reveal structural amorphization and phase transitions.
- Challenges traditional Al-intercalation models for metal selenide cathodes.

ARTICLE INFO

Keywords:
Cobalt selenide (CoSe)
Rechargeable aluminum batteries
Conversion mechanism
Selenium redox
Operando X-ray absorption spectroscopy
Synchrotron diffraction
Cobalt dissolution
Cathode degradation

ABSTRACT

Cobalt selenide (CoSe) has been explored as a cathode material for rechargeable aluminum batteries, particularly under high current densities (1 A g^{-1}) with a reported capacity of near 250 mAh g^{-1} at 5 A g^{-1}. However, its rapid capacity fading has hindered practical applications, and the underlying mechanisms proposed to be attributed to the intercalation of Al^{3+} remain unclear. In this study, CoSe was synthesized via high-temperature selenization of a ZIF-67 MOF template, and its electrochemical behavior was investigated using *operando*, *in situ* and *ex situ* characterization techniques. Contrary to the previously accepted Al^{3+} intercalation mechanism, we reveal a complex, partially reversible conversion mechanism driven by selenium redox activity. *Operando* synchrotron diffraction and X-ray absorption spectroscopy show a phase transition from hexagonal CoSe to cubic $CoSe_2$, alongside selenium oxidation from Se^{2-} to $(Se_2)^{2-}$. Cobalt remains electrochemically inactive but undergoes structural reorganization and dissolution, forming soluble chloroaluminate complexes that migrate to the Al anode. This process contributes to capacity fade and anode contamination, as confirmed by *ex situ* SEM-EDX and ICP-OES. At high current densities, the desired electrochemical reactions outpace parasitic side reactions, preserving activity. These findings redefine the charge storage mechanism in CoSe and provide a framework for designing more stable cathodes for long-term RAB performance.

1. Introduction

According to the International Energy Agency's 2023 forecast, renewable electricity generation is expected to increase by nearly 70% from 2022 levels, reaching approximately 14,400 TW h by 2028 [1]. Despite the growth, the intermittency and climate-dependency most renewable energy sources pose challenges for grid stability and cost-effectiveness. Electrochemical energy storage systems, such as batteries and supercapacitors, make renewable energy a reliable source of electrical power [2], and save power costs by storing electrical energy

* Corresponding author.
E-mail address: ecfuentesm@unal.edu.co (E. Fuentes-Mendoza).

https://doi.org/10.1016/j.jpowsour.2026.240246
Received 5 January 2026; Received in revised form 15 April 2026; Accepted 25 April 2026
Available online 29 April 2026

during off-peak hours when it is cheaper, to use it at peak hours [3].

Secondary batteries offer high efficiency (70-90%) and fast response times, making them suitable for applications ranging from small devices to grid-scale storage [4,5]. Lithium-ion batteries (LIBs) dominate the market due to their performance, but concerns over the limited availability and uneven global distribution of lithium (Li) have prompted the search for alternative chemistries, especially for stationary energy storage [6].

Table 1 compares key properties of several candidate elements for battery systems, including Li, sodium (Na), potassium (K), magnesium (Mg), calcium (Ca), zinc (Zn), and aluminum (Al). Among these, Al stands out due to its high abundance, stability and high theoretical capacity, 8040 mAh cm^{-3} and 2980 mAh g^{-1} for plating and stripping [9]. These values exceed those of Li (3860 mAh cm^{-3} and 2760 mAh g^{-1}) [10], making Al a compelling candidate for next-generation batteries. However, progress in rechargeable aluminum batteries (RABs) development has been hindered by the corrosive nature of the required electrolytes [11–14].

RABs typically employ aluminum chloride ($AlCl_3$): 1-Ethyl-3-methylimidazolium chloride (EMImCl) ionic liquid electrolytes, where charge storage occurs via a dual-ion mechanism: reversible plating and stripping of metallic Al at the anode and insertion/disinsertion or conversion of the $AlCl_4^-$ anions at the cathode. Designing stable and high-capacity cathode materials for RABs remains a major challenge. Carbon-based materials, particularly graphite, exhibit excellent stability and cycling performance, but possess low specific capacity, especially at high current densities [15–22]. Polymer-based materials show promising activity but require conductivity enhancement strategies [23–25]. Transition metal oxides and chalcogenides deliver high initial specific capacity but degrade rapidly due to dissolution and structure instability [26–33]. To address chalcogenide and oxide degradation, heterostructures have been developed to suppress active material and improve cycling performance [13,34–39].

Among transition-metal chalcogenides, CoSe has attracted attention for its tunable morphology and electrochemical versatility, which are highly dependent on the synthesis methods. It has been successfully applied in various systems, including oxygen reduction catalysts [8], zinc-air batteries [40], and sodium-ion batteries [41]. Furthermore, CoSe has also been explored as a cathode material for RABs [42,43], but suffers from rapid capacity fading. Strategies, such as the incorporation of reduced graphene oxide [42] and MXenes layers [44], have been employed to improve stability. However, the fundamental mechanisms governing its charge storage and degradation remain unclear.

Previous studies on CoSe or $CoSe_2$, such as those by W. Xing et al. [43], Cai et al. [42] and Yao et al. [44], suggest that Al^{3+} ions are the primary charge carrier involved in the energy storage mechanism, with mechanisms ranging from Al^{3+} intercalation to conversion reactions involving Al^{3+}. In such mechanisms, one would expect Al^{3+} insertion at low potentials (discharge) and disinsertion at high potentials (charge). However, if the active species were instead chloroaluminate ions ($AlCl_4^-$), the reverse behavior would occur, insertion at high potential and disinsertion at low potentials. Moreover, Yao et al. identified cobalt (Co) dissolution and shuttling as key contributors to rapid capacity loss [44]. These findings highlight the need for a deeper understanding of the electrochemical processes and degradation pathways in CoSe.

In this study, we use CoSe as a model transition metal chalcogenide system to investigate the fundamental mechanisms of charge storage and degradation in RABs, rather than to propose Co-based materials for future applications. We challenge the accepted charge storage mechanism and charge carrier, hypothesizing that the dominant charge carrier is the bulkier $AlCl_4^-$. This proposition inverts the expected electrochemical behavior, suggesting anion insertion at high potentials and deinsertion at low potentials. A comprehensive approach is employed, combining electrochemical testing, *ex situ* analysis, and advanced *in situ* and *operando* synchrotron-based characterization techniques. Our investigation focuses on three key aspects: (i) Electrochemical activity and reversibility: using galvanostatic cycling with potential limitation (GCPL), cyclic voltammetry (CV), and chronoamperometry (CA). We distinguish between reversible and irreversible processes and assess the contributions of charge storage processes and side reactions. (ii) *In situ* and *Operando* structural transformations: through *in situ* XAS and *operando* synchrotron diffraction (SRD) and X-ray absorption spectroscopy (XAS), we analyze phase transitions and local electronic and structural rearrangements during cycling, particularly the transition from CoSe to $CoSe_2$ and the potential dissolution of Co. (iii) *Ex situ* degradation products: scanning electron microscopy coupled with energy dispersive X-ray spectroscopy (SEM-EDX) is used to assess the migration of Co species to the anode, Raman and XRD are used to characterize structural degradation of the cathode.

By integrating these aspects, we aim to establish a comprehensive understanding of the electrochemical mechanism in CoSe, laying the groundwork for the optimization of transition metal chalcogenides as potential cathode materials for RABs.

Table 1
Relevant properties of Li, Na, K, Mg, Ca, Zn, and Al [7–9].

	Redox potential (V vs SHE)	Ionic radius (pm)	Abundance in earth's crust (mg/kg)	Theoretical specific capacity (Ah g^{-1})
Li	−3.05	90	20	3.86
Na	−2.71	116	23,600	1.16
K	−2.92	152	20,900	0.68
Mg	−2.37	86	23,300	2.20
Ca	−2.87	114	41,500	1.34
Zn	−0.76	88	70	0.82
Al	−1.66	68	82,300	2.98

2. Experimental procedure

Synthesis of ZIF-67 Template: ZIF-67 was synthesized according to a reported procedure [45]. Briefly, a solution of 0.45 g $Co(NO_3)_2{\cdot}6H_2O$ (98 %, Sigma Aldrich) in 3 mL deionized (DI) water was rapidly added to a solution of 5.5 g 2-methylimidazole (99 %, Sigma Aldrich) in 20 mL DI water under stirring. The resulting purple mixture was stirred for 18 h at room temperature. The precipitate was collected by centrifugation, washed three times with a 1:1 v/v water/methanol mixture, and vacuum-dried at 80 °C for 24 h.

Synthesis of CoSe: CoSe was prepared via selenization of the ZIF-67 precursor, according to a reported procedure [43]. The as-synthesized ZIF-67 was thoroughly ground with selenium (Se) powder (99 %, Sigma Aldrich) in a 1:2 M ratio. The mixture was then annealed in a tubular furnace under an inert atmosphere using a two-step protocol: first, heating to 350 °C at 5 °C min^{-1} with a 2-h hold to form $CoSe_2$, followed by a second annealing at 800 °C for 2 h. This high-temperature step converted $CoSe_2$ to CoSe and carbonized the organic framework into a conductive carbon matrix. *Note: Excess Se sublimation during annealing necessitates the use of a long furnace tube and regular monitoring to prevent blockages.*

Electrolyte Preparation: The ionic liquid electrolyte ($AlCl_3$(99.99%, Sigma Aldrich): EMImCl (95%, Sigma Aldrich), 1.3:1 M ratio) was prepared in an argon-filled glovebox (MBraun, <0.1 ppm H_2O and O_2) by alternately adding small amounts of the components in a glass vial under constant stirring.

Electrode fabrication: The cathode slurry was formulated with 80 wt% CoSe powder, 10 wt% carbon black (P65, MTI), and 10 wt% poly (acrylonitrile) (Mw: 150,000, Sigma Aldrich) binder (3 wt% solution in N, N-Dimethylformamide (99.9 %, Avantor)). The slurry was cast onto carbon paper (120 μm, Quintech) and dried overnight at room temperature. Electrodes were punched into appropriate sizes (2 × 2 cm squares for pouch cells; 12 mm in diameter disks for Swagelok cells) and vacuum-dried at 90 °C for 12 h prior to use. The typical active material loading was 1.2 mg cm^{-2}.

Cells fabrication: To mitigate the risk of corrosion from the highly acidic electrolyte and considering the susceptibility of the current molybdenum collector to corrosion [3], Swagelok-type cells were constructed using chemically resistant tungsten bars and a Teflon body. Cells were assembled using a CoSe cathode, two glass fiber separators (D-GF, Whatman), and an Al foil (0.075 mm, 99.0 %, Goodfellow) counter electrode. Electrolyte volumes of 250 µL and 800 µL were used for Swagelok and pouch cells, respectively.

Electrochemical characterization: Electrode performance was evaluated using Cyclic Voltammetry (CV) at 20 mV s^{-1} between 0.3 and 2.3 V. Galvanostatic cycling with potential limitations (GCPL) was performed at current densities of 25 mA g^{-1} and 1 A g^{-1} within a 0.3-2.3 V window. Two chronoamperometry (CA) protocols were used: (i) at a constant 2 V for 2 h for pretreatment procedures (post-CA procedures are detailed in the Results and Discussion), or (ii) using a multi-step voltage protocol (from 1.2 V to 2.5 V and back to 1.2 V) with 11.5-min holds for *in situ* XAS studies. Linear Sweep Voltammetry (LSV) at 0.5 mV s^{-1} from 0.1 to 2.5 V using inert carbon paper cathodes to assess electrolyte stability with pristine and pre-treated electrolytes (pre-treatment procedures are detailed in Results and Discussion).

Material Characterization: Pristine and cycled (*ex situ*) electrodes were characterized by X-ray diffraction (XRD, STOE Stadi-P, Mo Kα1 radiation), Raman spectroscopy (Horiba LabRam, 633 nm laser), and XAS (Co and Se K-edges, easyXAFS300+, with Mo X-ray tube, monochromators: Si533 for Co and Ge844 for Se). *Ex situ* samples were retrieved from disassembled cells in a glovebox, washed with 1,2-difluorobenzene (unless otherwise specified), and vacuum-dried at room temperature for 12 h. Data were processed using FullProf (XRD) and Demeter (XAS) software suites. Co dissolution was quantified by inductively coupled plasma optical emission spectrometry (ICP-OES, PerkinElmer OPTIMA 4300DV) after soaking CoSe in the electrolyte for 12 h.

Operando Characterization: Operando SRD and XAS data were collected at Deutsches Elektronen-Synchrotron (DESY) during the cycling of pouch cells at 1 A g^{-1} (0.1-2.3 V). SRD measurements (λ = 0.207337 Å) were performed at the beamline P02.1 [46], with LaB_6 (660c NIST standard) for calibration. Diffraction data were collected using the Varex XRD 4343 C T (150 × 150 μm^2 pixel size, 2880 × 2880 pixel area, CsI scintillator directly deposited on amorphous Si photodiodes) and azimuthally integrated using the DAWN software [47]. XAS data were collected at beamline P65 in the Co K-edge.

3. Results and discussion

3.1. Electrochemical activity and reversibility

Fig. 1 presents the characterization of the synthesized CoSe. Fig. 1A shows the Raman spectrum of CoSe. The D band, at approximately 1360 cm^{-1}, corresponds to the breathing modes of sp^2 carbon rings. It indicates disordered or amorphous carbon. The G band, at 1590 cm^{-1}, is attributed to the in-plane vibrational mode of sp^2 hybridized carbon atoms, represents graphitic domains. The calculated I_D/I_G ratio suggests a moderately ordered carbon matrix with limited defects. A sharp peak at 675 cm^{-1} was assigned to C-Se bonding [48]. Additional bands at 468 and 507 cm^{-1} are attributed to Co-Se vibrations, further confirming the formation of the CoSe phase [49]. Minor shifts from literature values are attributed to differences in stoichiometry and morphology.

Fig. 1B shows the XRD pattern of CoSe; the reflections are indexed to the hexagonal phase (space group $P6_3/mmc$). This result is consistent with the findings reported by Wing et al. [43], confirming the successful synthesis of CoSe. The Rietveld refinement yielded lattice parameters of a = b = 3.61937 ± 0.00007 Å and c = 5.30124 ± 0.00018 Å, where Co atoms form the metallic sublattice and Se occupies the interstitial sites.

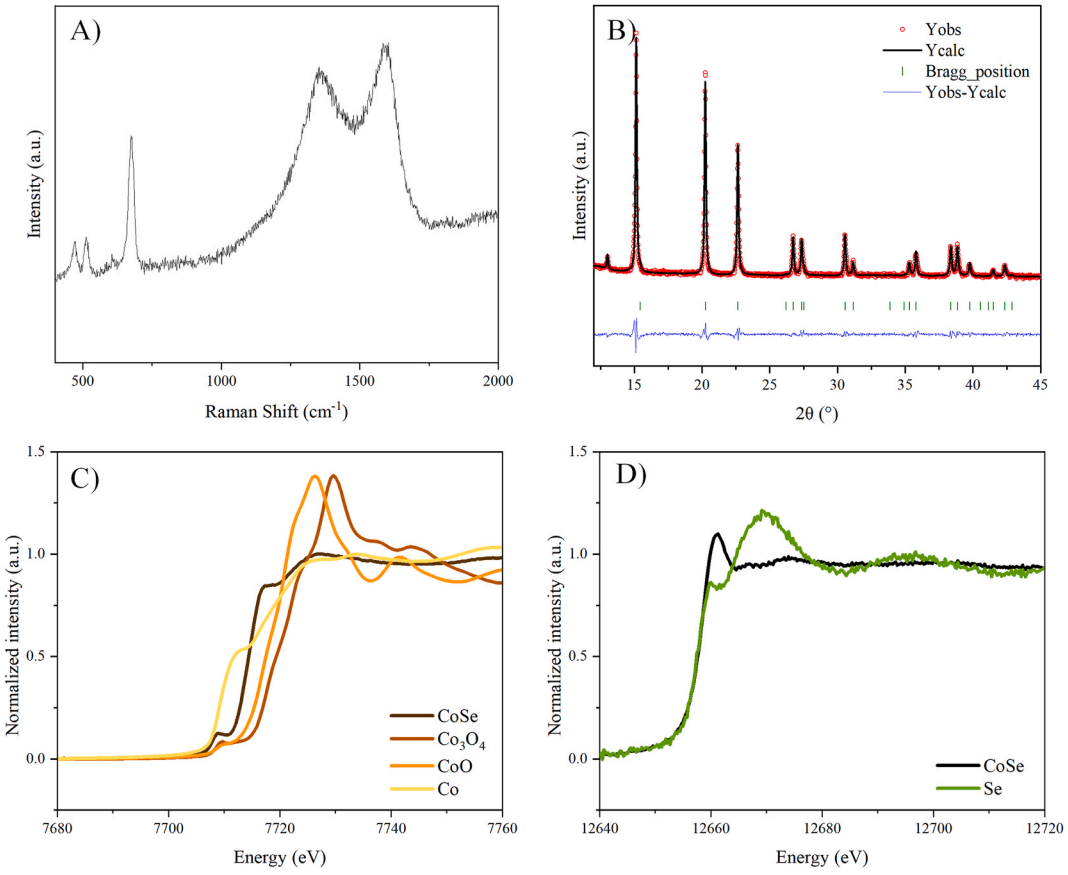

Fig. 1. Characterization of CoSe: A) Raman spectra, B) X-ray diffraction pattern of CoSe (R_{wp}: 5.08 R_{exp}: 2.73 χ^2: 3.45). C) XAS spectra of CoSe Co K-edge, D) Se K-edge.

Additionally, a minor secondary phase, attributed to $CoSe_2$, was detected. This phase crystallizes in a cubic system (space group *Pa-3*) with a refined lattice parameter of $a = b = c = 5.8727$ Å. Quantitative phase analysis estimated the composition to be $99.81 \pm 0.01\%$ for the primary hexagonal CoSe phase and $0.19 \pm 0.01\%$ for $CoSe_2$. Due to this being near the detection limit, and its negligible impact on the refinement quality, its presence in the pristine sample should be interpreted cautiously. However, as this phase becomes more prominent after cell assembly, as will be further discussed in the *operando* analyses, its formation appears to be electrolyte-induced and is proven to play a role during cycling.

The XAS spectrum at the Co K-edge is presented in Fig. 1C. As expected, Co^0 exhibits the lowest energy absorption edge. CoSe and CoO exhibit a slight edge shift to higher energy, consistent with a Co^{2+} oxidation state, while Co_3O_4 displays the most pronounced shift, reflecting its mixed Co^{2+}/Co^{3+} valence. The XAS spectrum at the Se K-edge (Fig. 1D) shows a minimal shift compared to elemental Se. Literature reports that the K-edge position for Se compounds varies within a narrow range [50]. However, the white line of Se^0 reference, located at approximately 12,669 eV, has a slightly higher intensity compared to that for the CoSe (12,660 eV). The intensity and slight shift of the white lines suggest a reduced oxidation state in CoSe compared to elemental Se, consistent with literature trends [51]. These findings are consistent with the covalent nature of the Co-Se bond and align with previous studies on cobalt selenides (CoSe and $CoSe_2$) [52,53].

The electrochemical characterization is reported in two main approaches: i) direct measurements conducted on the cell in its pristine, as-assembled state, and ii) measurements performed after an initial electrochemical pretreatment (CA), as detailed in a later section.

The direct measurements consist of CV and GCPL. As shown in Fig. 2A, the CV curves indicate that the first cycle exhibits two main reversible processes. The anodic peaks are observed at 1.03 V and 2 V. The process associated with the latter peak is incomplete due to the settled potential cutoff (2.3 V) to avoid electrolyte decomposition. The corresponding cathodic peaks appear at 0.57 V and 1.80 V. The following cycles show more pronounced peaks and a slight displacement of the anodic peaks towards lower voltages and cathodic peaks to higher voltages, for example, by the 10th cycle, the anodic peak is at 1.01 V and the associated cathodic peak at 0.66 V. This trend suggests a small reduction in overpotential and improved electrochemical reversibility, possibly indicating gradual activation of the electrode material, or the progressive remotion of the native Al_2O_3 during the initial cycles [54,55]. This layer initially impedes Al plating and stripping, but is gradually dissolved by the corrosive chloroaluminate electrolyte [56]. As the passive layer is stripped away, charge transfer improves, leading to reduced overpotentials and enhanced reversibility, as reflected in the evolution of the redox peaks. The development of the multistep redox process is more distinctly revealed in the differential capacity (dQ/dV) plots, which will be further discussed in the subsequent section.

In Fig. 2B, the measurement begins at the open-circuit voltage (OCV, 1.55 V) and proceeds toward lower potentials (discharge). The initial discharge capacity is negligible (~1 mAh g^{-1}), likely attributed to double-layer formation. While the subsequent charge reaches approximately 118 mAh g^{-1}. This pronounced asymmetry indicates that the CoSe electrode does not undergo significant reduction (cation insertion) during the initial discharge, and that charge storage becomes active only after an initial oxidation step.

In contrast, Fig. 2C, shows that when cycling starts from the OCV (1.73 V) toward higher potentials (charge), charge and discharge capacities in the first cycle are comparable (154 and 114 mAh g^{-1},

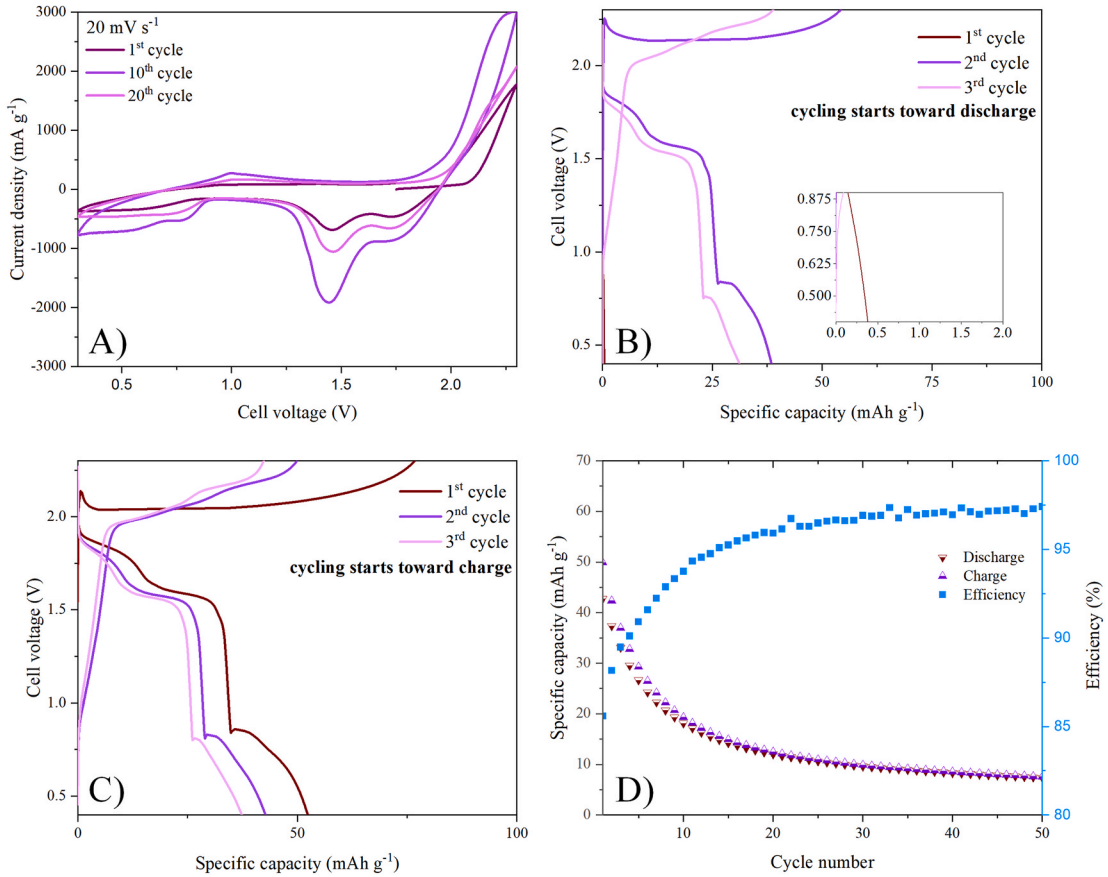

Fig. 2. *Electrochemical characterization*: A) CV curves cycling towards charge, B) GCPL curves starting from OCV toward lower potentials, C) GCPL curves starting from OCV toward higher potentials, D) Efficiency and specific capacity of cell start charging.

respectively). This behavior suggests that, once the electrode has been oxidized, reversible ion insertion and extraction can occur.

Taken together, these results imply that the CoSe electrode requires an activation process via oxidation before reversible electrochemical reactions can proceed. This behavior would rather suggest an anion-insertion mechanism, like the $AlCl_4^-$ insertion into graphite [18,20,57]. These results contradict earlier reports that identified Al^{3+} as the active species in the CoSe system.

Finally, the theoretical specific capacity of CoSe, assuming Al^{3+} conversion or intercalation with a three-electron redox process, is approximately 409 mAh g^{-1}. However, the experimentally observed capacity is considerably lower. This discrepancy can be attributed to a different charge storage mechanism dominated by the transfer of $AlCl_4^-$, rather than multivalent Al^{3+}. Since $AlCl_4^-$ involves single-electron redox reactions, this results in a reduced theoretical capacity (194 mAh g^{-1}), which is closer to our experimental results.

Fig. 2D shows the charge and discharge capacity and coulombic efficiency over the first 20 cycles, revealing notably low efficiency in the initial cycles. Some studies have attributed such behavior to the formation of a cathode-electrolyte interphase (CEI), particularly in graphitic cathodes [20,22,58]. While the synthesized CoSe includes a carbonaceous matrix derived from the MOF precursor, and thus the formation of a CEI cannot be entirely dismissed, its presence in selenide-based cathodes has not been widely reported.

The electrochemical evaluation of CoSe cathodes was conducted at relatively high current density (1 A g^{-1}), a strategy also adopted in previous studies on cobalt selenides [42–44]. Interestingly, when cells are cycled at a current density of 25 mA g^{-1}, they exhibit a prolonged, flat voltage plateau near 2 V, referred to as an “infinite plateau” as observed in Fig. S1. This behavior is characteristic of a dominant parasitic, side reaction, likely due to active material dissolution, that overshadows the intended electrochemical processes.

At low current densities, parasitic reactions surpass the electrochemical process, allowing them to proceed extensively. This observation explains the low initial coulombic efficiency and supports the hypothesis that the initial stages of cycling are dominated by dissolution of active species rather than by the formation of a CEI. Although these reactions are less visible at higher current densities, they still influence the initial capacity and reversibility.

To further investigate the nature of the processes occurring during the infinite plateau, CA at 2 V during 2 h was performed on three identical cells, each with slightly different active material masses (see Table S1). The current–time profiles presented in Fig. S2 deviate from classical Cottrellian behavior, which predicts a monotonic current decay. Instead, an initial current drop is followed by a distinct, gradual increase. The non-Cottrellian response suggests the prevalence of complex Faradaic processes over simple double-layer charging. We attribute the rising current to parasitic oxidation reactions, likely driven by the dissolution of active material (e.g., Co or Se species) into the electrolyte. These dissolved species can become electrochemically active in the bulk solution, leading to sustained Faradaic currents that mask the stabilization expected from capacitive processes [59].

The parasitic reaction is in agreement with the findings of GCPL experiments at low current densities, where the voltage profile forms an infinite plateau, suggesting a prolonged oxidation process that could involve more than just charge storage.

The measurements performed after the CA pretreatment were employed to assess the impact of the parasitic oxidation process on the performance and the contribution of the parasitic reaction to the capacity. Four electrochemical protocols were applied:

Cell 0 (Control): No CA. GCPL at 1 A g^{-1} performed directly after assembly.

Cell 1: CA at 2 V for 2 h, followed by GCPL at 1 A g^{-1}.

Cell 2: CA at 2 V for 2 h, followed by replacing the electrolyte and separator with fresh, unused components before performing GCPL at 1 A g^{-1}.

Cell 3: CA at 2 V for 2 h, followed by replacing the electrolyte, separator, and Al foil with fresh, unused components before performing GCPL at 1 A g^{-1}.

Fig. 3 compares the cycling behavior of these cells. In Fig. 3A it can be observed that while Cell 0 begins with the highest initial specific capacity (~200 mAh g^{-1}), it suffers rapid degradation, stabilizing at only ~16 mAh g^{-1} by the 100th cycle. In contrast, Cell 3 starts with a much lower initial capacity (~11 mAh g^{-1}) but exhibits superior stability, reaching ~31 mAh g^{-1} after 100 cycles. This trade-off highlights the dual nature of the high-voltage process: while it contributes to initial capacity, it also initiates degradation pathways, most likely altering the electrolyte composition, compromising long-term performance. The pretreatment protocols, particularly the complete replacement of cell components in Cell 3, appear to mitigate these effects, enabling a more stable and durable cycling behavior. Notably, the difference in capacity between Cell 0 and GCPL curves starting from OCV toward higher potentials is attributed to the binder used for the fabrication of the electrodes (See Fig. S3).

To further dissect the electrochemical behavior, dQ/dV plots were generated for all four cells (Fig. 3B–F). These plots provide a high-resolution view of the redox processes and their evolution over cycling.

In Cell 0 (Control, Fig. 3C) an immediate and intense activation is observed. The high voltage oxidation processes evolve from multiple peaks in the first cycle into a single, high-intensity peak. The rapid activation is accompanied by the abrupt degradation and poor capacity retention. Conversely, Cell 1 (Fig. 3D): presents significantly lower peak intensity and a gradual reduction in the overpotential over cycling, indicating improved kinetics but limited capacity attributed to the consumption of active species in the electrolyte by the parasitic reaction. Cell 2 (Fig. 3E) presents similar behavior to Cell 1 but with higher peak intensity, reflecting a more robust electrochemical process, likely enabled by electrolyte replacement, supporting the theory that the parasitic reaction at 2.0 V consumes active species in the electrolyte. Finally, Cell 3 (Fig. 3F) shows a slow, steady activation, rather than a rapid, destructive one, highlighting the enhanced stability, attributed to the replacement of electrolyte and Al anode. This observation demonstrates that the irreversible process at 2.0 V not only consumes active species in the electrolyte but also affects the surface of the Al anode.

Another interesting feature observed along the four cells is the reduction peak near 0.85 V, observed in Cells 0 and 2 during the first cycle (Fig. 3B), but absent in Cells 1 and 3. In subsequent cycles, the evolution of this peak differs across the cells. In Cell 3, during the first cycle, the passivation layer on the fresh Al anode is restored, and in the subsequent cycles, it is gradually removed, leading to the delayed appearance of the 0.85 V peak. In contrast, Cell 1 shows no such recovery, likely because the electrolyte becomes depleted in $AlCl_4^-$ due to its consumption in side reactions during CA. Conversely, the peak is not visible in Cell 1 and decreases progressively in Cell 2 to eventually disappear upon cycling. Based on these observations, the 0.85 V peak can be attributed to Al stripping, as it aligns with the Al mechanism proposed by Appiah et al. in which Al stripping occurs through the transport of $Al_2Cl_7^-$ from the bulk electrolyte to the anode interface, where it is converted into $AlCl_4^-$ and Cl^-, which are then transported back into the bulk [56]. This interpretation is further supported by the time-dependent effect of electrolyte contact on the removal of the insulating oxide layer from the Al anode, as studied by F. Rahide et al. [54].

The irreversible capacity loss and distinct electrochemical features observed at high voltages suggest the occurrence of an initial irreversible transformation. This process is characterized by the appearance of a reduction peak near 0.8 V, which serves as a signature of electrode activation. While this reaction is essential for enabling the main charge-storage mechanism, it also triggers degradation pathways that, if left uncontrolled, lead to rapid performance decay, as observed in the control cell. However, when properly managed through electrode pretreatment and component replacement, this transformation can act as a

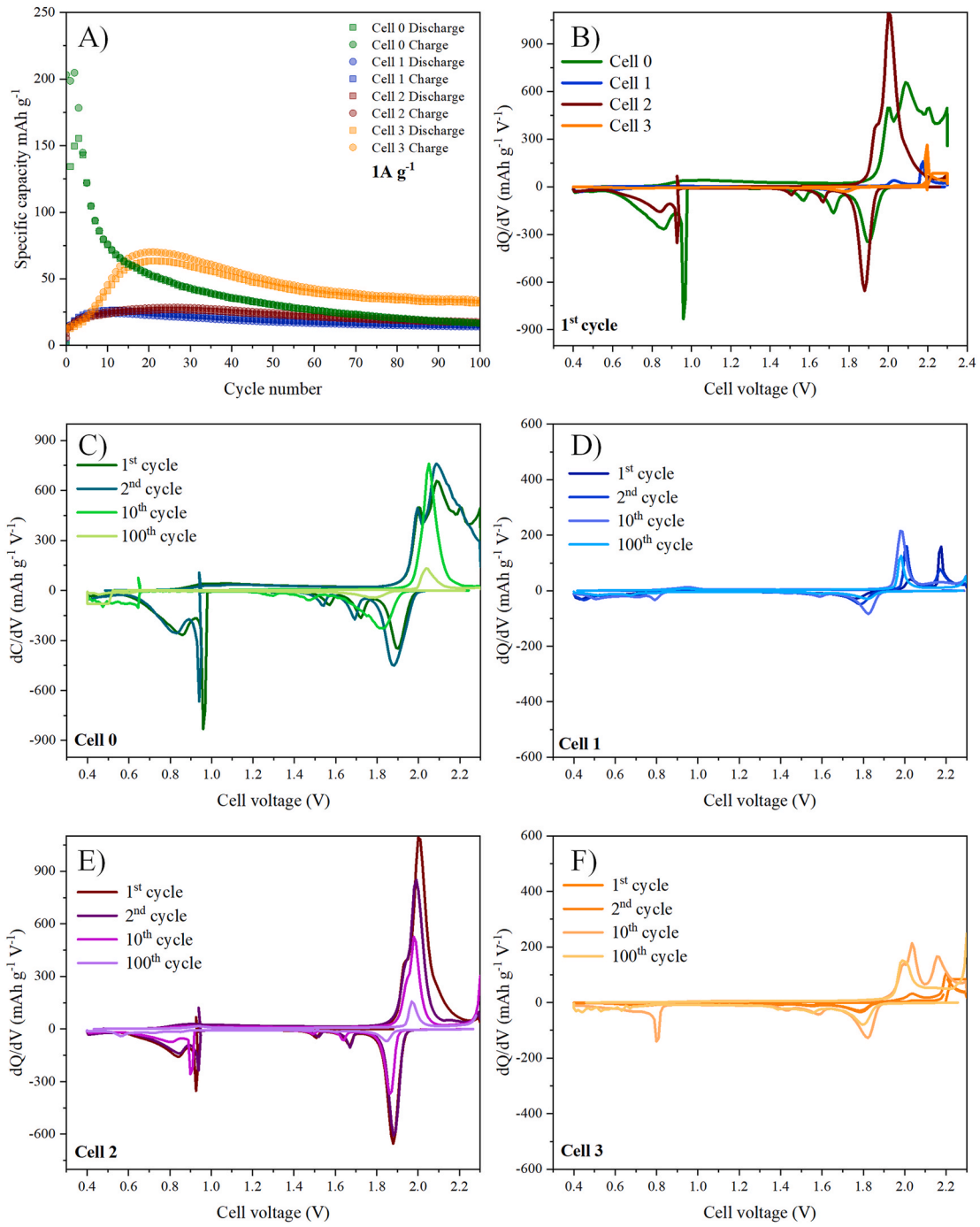

Fig. 3. High Voltages Irreversibility. Electrochemical Characterization of Al//CoSe Cells with and without CA Pretreatment A) capacity vs. cycle number. Differential capacity (dQ/dV) plots B) 1st cycle C) Cell 0 D) Cell 1, E) Cell 2. F) Cell 3.

beneficial activation step, as demonstrated by the improved performance of Cell 3.

Based on these results, we propose that the high-voltage irreversibility involves a dual process encompassing both activation and degradation. This behavior likely arises from two simultaneous mechanisms: First, the irreversible conversion of CoSe: near 2 V, CoSe undergoes a one-time conversion reaction, possibly forming $Co_x(AlCl_4)_y$, consistent with observations reported in KCl-$AlCl_3$ melts [60]. Second, the dissolution and shuttling of Co species: The Co species generated during this initial step gradually dissolve into the electrolyte and migrate toward the anode. This leads to active material loss, partial electrical isolation of CoSe particles, and contamination of the Al anode surface, contributing to capacity fading over cycling. This hypothesis will be further examined below by ex situ analyses.

The ability to control this initial process, either by suppressing it or by isolating it from long-term cycling, is critical for achieving both high performance and extended cycle life in CoSe-based RABs.

3.2. *In situ and operando structural transformations*

The *operando* SRD data provide a comprehensive view of the structural transformations occurring in CoSe cathodes during cycling.

The most prominent observation is the progressive broadening and reduction in the intensity of all reflections associated with the hexagonal

CoSe phase (space group $P6_3/mmc$), suggesting a progressive amorphization of the structure. The loss of long-range order suggests that the crystalline CoSe structure is being consumed and replaced by less ordered or amorphous products (Fig. S4). In addition, the appearance of new reflections corresponding to $CoSe_2$ and Co_3Se_4 (space groups *Pa-3* and *C 1 2/m 1*, respectively) phases is observed, supporting an initial irreversible transformation process. For better understanding, the phase transformation is divided into two interconnected phenomena: monotonous conversion reaction and transient structural changes.

Monotonous conversion reaction: Characterized by the systematic decrease in intensity of reflections belonging to the original CoSe phase, directly correlated with the growth of reflections from a new $CoSe_2$ phase, as observed in Fig. 4A and B. The reflection at 4.43° (CoSe (101)) gradually diminishes until its complete disappearance, while a new reflection at 4.52° ($CoSe_2$ (210)) intensifies (Fig. 4A). A similar trend is observed for the CoSe (110) reflection at 6.64°, which fades as the $CoSe_2$ (311) peak at 6.71° grows. The reciprocal behavior is indicative of a well-defined crystalline-to-crystalline phase transition, indicating that the charge storage mechanism involves a chemical transformation rather than ion insertion into a stable host lattice. This supports the hypothesis that the initial activation of the cathode involves a structural transformation of the CoSe, forming new phases and possibly releasing soluble Co species into the electrolyte.

Transient structural changes: In contrast to the well-ordered conversion, other regions of the diffractogram exhibit highly dynamic and transient behavior. These fluctuations suggest the formation and dissolution of intermediate species that are metastable, as observed in Fig. 4C and D. Disorganized changes in reflections corresponding to CoSe (301), (204), and (105), $CoSe_2$ (433), and multiple overlapping reflections from Co_3Se_4 (Fig. 4C). Seemingly reversible amorphization of the $CoSe_2$ (733) reflection at 16.61°, followed by the transient emergence of reflections likely associated with Co_3Se_4 phase (Fig. 4 D). The transient appearance of Co_3Se_4 reflections indicate that the charge storage mechanism in CoSe cathodes is not a simple one-step process. Instead, it involves multiple intermediate phases, transient species, and competing structural transformations.

Finally, although it is not the primary focus of this study, *operando* SRD data also reveal structural changes in the Al foil anode, as shown in Fig. S5 the observed dynamic behavior in the Al-dominated regions during cycling remains uncertain and is not attributed to specific phase transformations at the Al lattice due to the bulk nature of XRD and the early stage of cycling.

To gain deeper insights into the evolution of oxidation state and local structural changes of CoSe during cycling, *operando* XAS at the Co K-edge was conducted. This technique enables the monitoring of subtle electronic and structural transformations that occur during charge and discharge. The results are presented in Fig. 5 (charge/discharge curve is presented in Fig. S6).

Fig. 5A presents the initial Co K-edge XANES spectra of CoSe, alongside reference spectra of elemental Co and cobalt oxides. CoSe presents the same edge position as the pristine sample (Fig. 1C), relative to the reference, indicating a stable oxidation state of Co. Fig. 5B shows the cascade of Co K-edge XANES spectra collected during cycling. Notably, no significant shift in the absorption edge is observed throughout the charge and discharge process. The absence of any substantial edge shift indicates that Co remains predominantly in its pristine oxidation state + II, suggesting it does not serve as the primary redox center within the CoSe framework during cycling. This finding strongly suggests that the electrochemical activity of the CoSe cathode is primarily driven by Se redox processes. While the inactivity of Co is observed within this specific host structure, it might exhibit different electrochemical activity if evaluated as a standalone component or within a different coordination environment, though further evidence is required to confirm these secondary interactions.

Fig. 5C shows the Fourier-transformed extended X-ray absorption fine structure (EXAFS) spectra during the first charge process. Although no major changes in Co oxidation state are observed, the local structural environment of Co is noticeably altered. Particularly, a reduction in the amplitude of the first coordination shell, corresponding to the Co-Se bond, suggests an increase in structural disorder, likely due to Co dissolution and migration during charging. Similarly, Fig. 5D presents the EXAFS spectra during the first discharge process. The data show that the previously observed structural disorder is only partially reversible. These results are consistent with the *operando* SRD results, which indicated a phase transition from CoSe to $CoSe_2$ and Co_3Se_4, accompanied by amorphization but without significant Co oxidation beyond the Co^{2+} state.

For *in situ* XAS at the Se K-edge, three sequential measurements, each lasting 5 min, were conducted at constant voltages throughout the first cycle. The resulting spectra were averaged and smoothed to reduce noise and facilitate interpretation. The processed curves are presented in Fig. 6. Due to the pouch cell configuration, significant background interference from other cell components was present, particularly in the pre-edge and post-edge regions. Moreover, it is important to note that the Se K-edge position for Se^{2-} compounds varies within a narrow range, typically between 12656.0 eV (CuSe) and 12658.0 eV (SeS_2) [50].

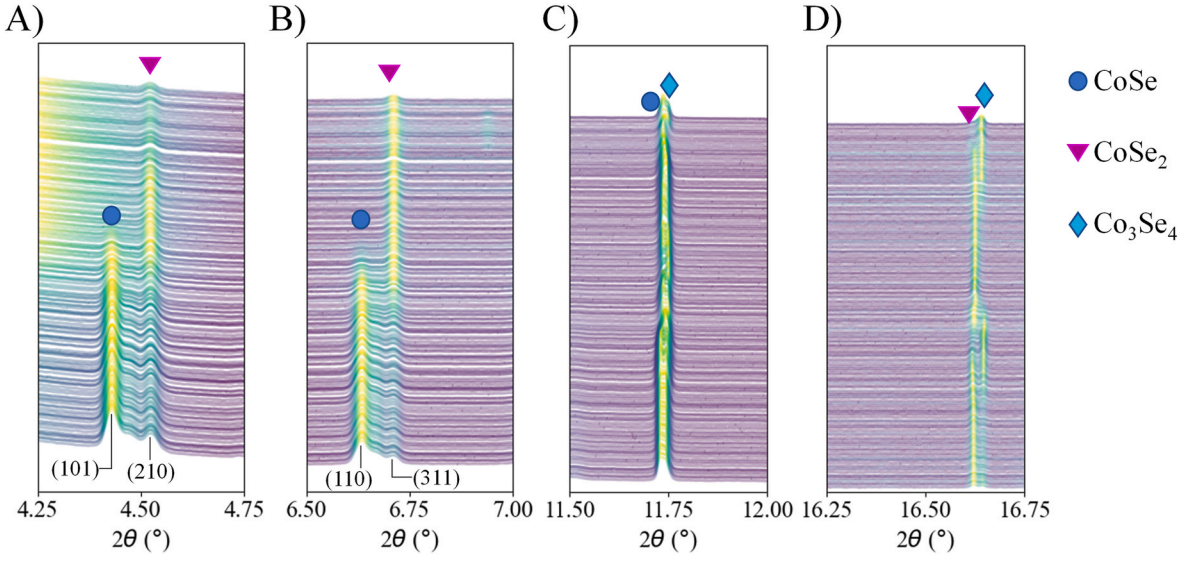

Fig. 4. Operando SRD diffractograms A) 2θ = 4.5°–4.75°, B) 2θ = 6.5°–7, C) 2θ = 11.5°–12°, D) 2θ = 16.25°–16.75°.

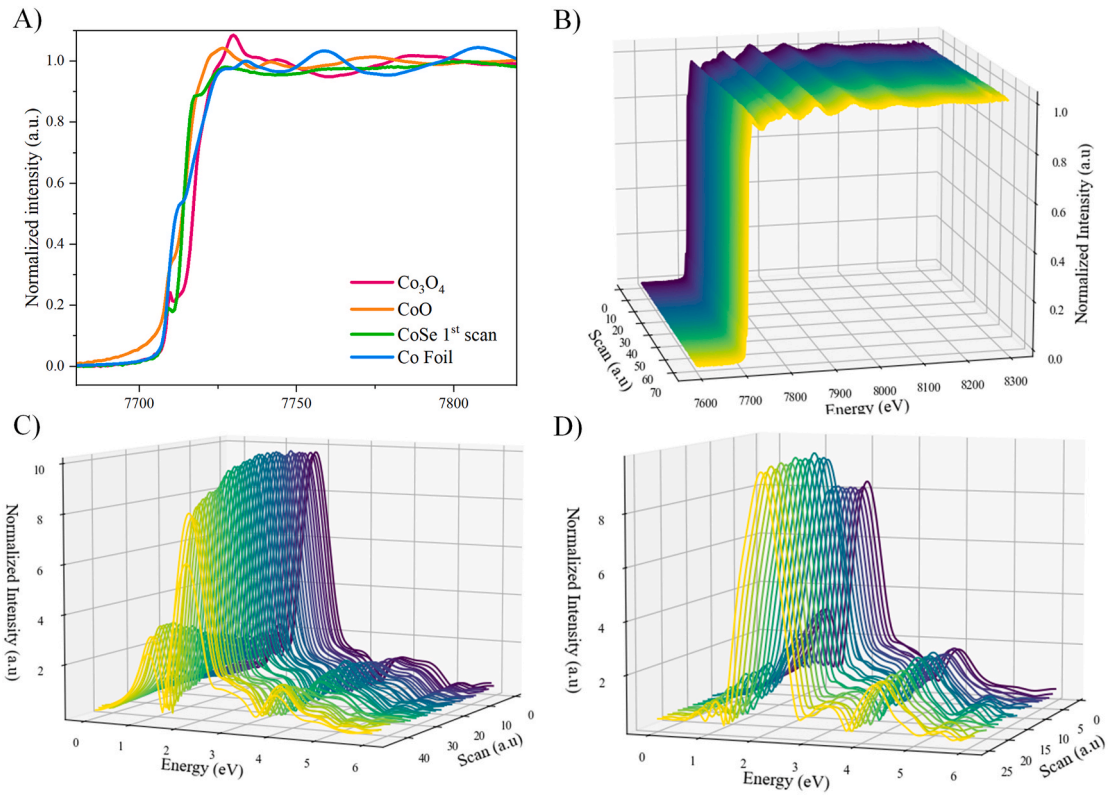

Fig. 5. Operando XAS: A) Co K-edge XANES spectra of the CoSe 1st scan Co foil, Co_3O_4 and CoO B) operando XAS Co-edge spectra, C) FT EXAFS spectra for the initial charge, D) FT EXAFS spectra for the initial discharge.

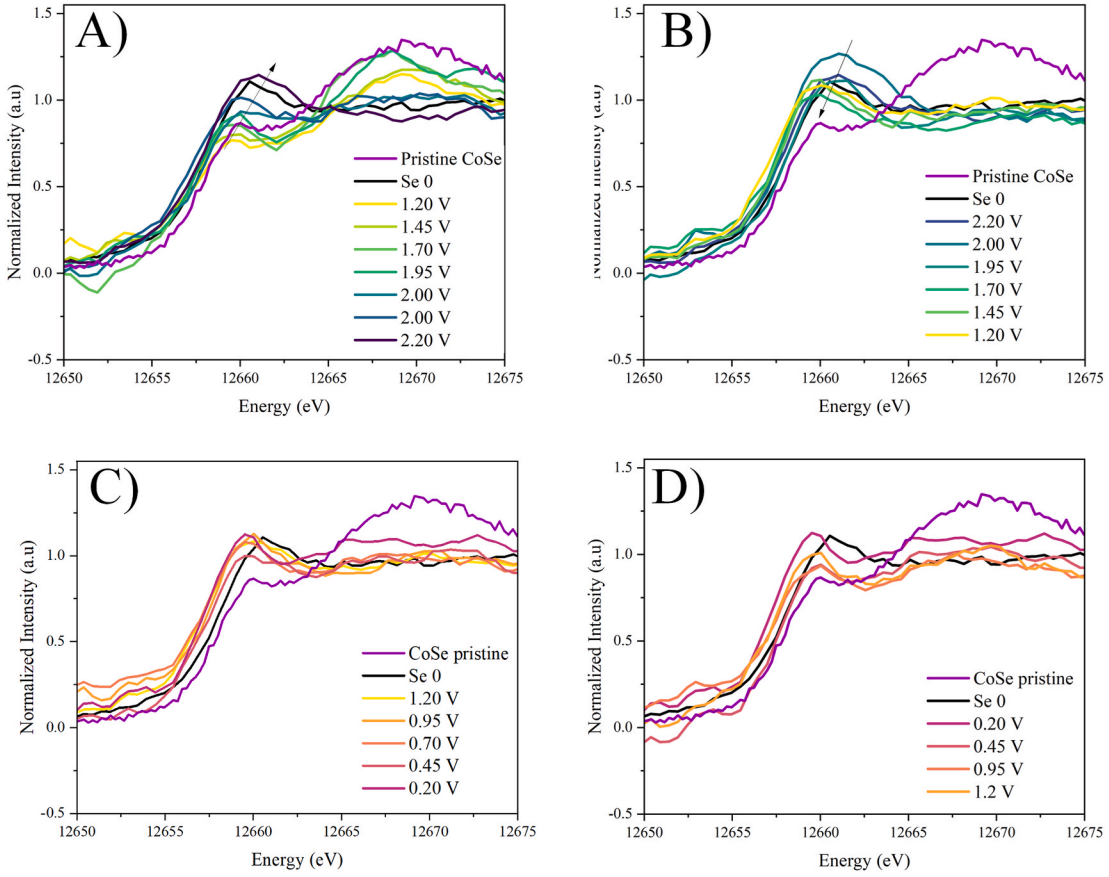

Fig. 6. In situ Se K-edge XAS spectra of CoSe cathode for the first cycle A) from OCV to 2.2 V B) from 2.2 to 1.2 V C) from 1.2 to 0.2 V D) from 0.2 to 1.2 V.

Therefore, significant shifts were not expected. However, despite these limitations, more pronounced changes were observed in the white-line region (edge maxima). Both the energy and intensity of the white line increase upon charging and decrease during discharge. This behavior aligns with findings by Olegario et al. [51], who demonstrated that the Se K-edge white-line intensity and position correlate with the oxidation state of Se. As a result, the analysis focuses on the rising edge region, where qualitative shifts in absorption energy can still be discerned.

During charging (Fig. 6A), a slight shift of the absorption edge to higher energies is detected approaching the energy position characteristic of elemental Se (Se^0), but given the differences in local bonding environments, this does not conclusively indicate oxidation to Se^0. The possibility of intermediate species, such as polyselenides $(Se_n)^{2-}$, cannot be ruled out, and it is supported by the $CoSe_2$ (Pa-3) structure, which inherently possesses Se-Se dimers, and may contribute to the observed spectral features. This shift reverses during discharge (Fig. 6), indicating a return toward the selenide (Se^{2-}) state.

The observed trend is consistent with a reversible redox process, where Se is oxidized during charging and reduced during discharge, confirming its role as the electrochemically active species in the CoSe

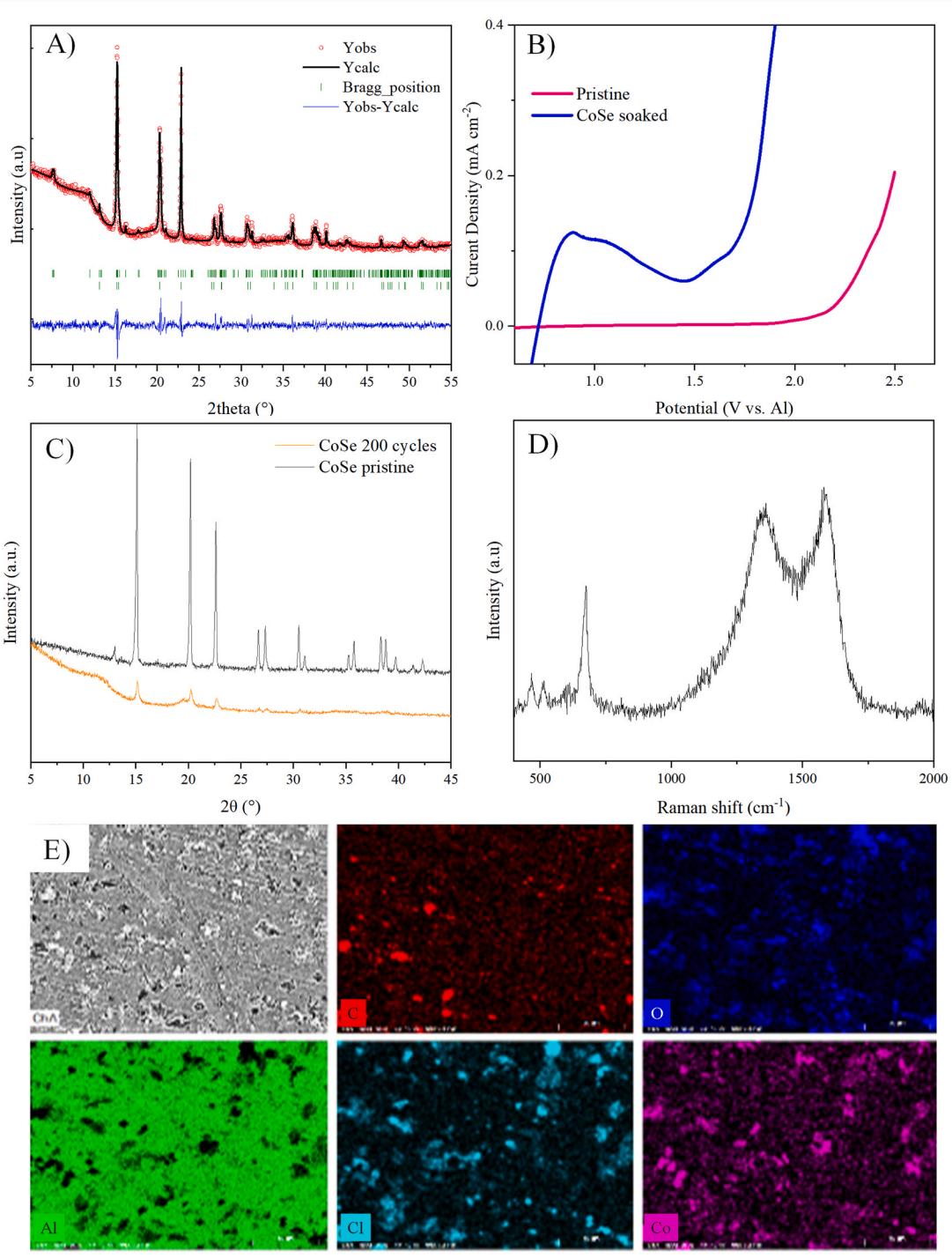

Fig. 7. *Ex situ* characterization: A) X-ray diffractogram of CoSe soaked in electrolyte (R_{wp}: 2.60, R_{exp}: 2.28, χ^2:1.31) B) LSV of CoSe soaked electrolyte, C) X-ray diffractogram of CoSe after 200 cycles, D) Raman spectra of CoSe after 200 cycles, E) SEM-EDX analysis of Al foil after 20 cycles.

cathode.

Based on our findings, we have proposed a previously unreported charge storage mechanism for CoSe in chloroaluminate ionic liquids. Contrary to the prevailing literature, which often attributes capacity to Co-based redox and Al^{3+} intercalation, our *operando* analyses reveal, for the first time, a mechanism where Se is reversibly oxidized during charging and reduced back upon discharging. This redox process is accompanied by a reversible reconstruction of the host Se framework, resulting in a structurally distinct yet stable lattice after the first cycle. Furthermore, we provide compelling evidence that Co, rather than participating in redox reactions, dynamically interacts with electrolyte anions to form a soluble cobalt chloroaluminate complex. While we propose a complex such as $Co(Al_2Cl_4)_2$, to illustrate the migration pathway, it is important to emphasize that the exact stoichiometry of these soluble complexes remains a hypothetical model and has not been demonstrated experimentally. This complex formation facilitates structural reorganization and is crucial for the reversibility of the Se-based redox couple.

3.3. Ex-situ degradation products

This section presents *ex situ* measurements that support and validate the proposed mechanism, offering additional evidence for the structural and chemical transformations occurring during and before cycling.

Operando characterization revealed that $CoSe_2$ is visible from the first measurement, suggesting that degradation may initiate even before electrochemical cycling. To investigate this, CoSe electrodes were soaked in pristine electrolyte. Visual inspection revealed a color change in the electrolyte, from translucent to yellowish, indicating chemical interaction. Subsequent ICP-OES analysis confirmed the presence of both Co and Se in the soaked electrolyte, providing direct evidence that CoSe dissolves upon contact with the electrolyte, even prior to cycling.

The soaked, unwashed CoSe electrode was analyzed via XRD. The resulting diffractogram, shown in Fig. 7A reveals significant changes compared to the pristine sample. The disappearance of the reflection at 13.08°, corresponding to the (100) plane, indicates anisotropic dissolution, disrupting the in-plane registry of the crystal. A general decrease in reflection intensity suggests partial dissolution of the material. Finally, a shift toward higher 2θ angles implies lattice shrinkage and defect formation, likely due to the loss of Co and Se atoms, as supported by ICP-OES data. Additionally, XRD measurements also revealed Co_3Se_4 reflections. This phase is present in the *operando* SRD data and was proposed as an intermediate species. The more prominent presence in the *ex situ* measurement can be associated with the exposure of the sample to air. Their presence underscores the importance of *in situ* and *operando* techniques, which avoid such artifacts and provide more reliable insights into real-time transformations. The Rietveld refinement yielded lattice parameters of $a = b = 3.57475 \pm 0.00015$ Å and $c = 5.28828 \pm 0.00073$ Å for the CoSe phase, confirming the lattice shrinkage. Moreover, the quantitative analysis reveals that in the soaked sample, the hexagonal CoSe phase corresponds to 39.04 ± 1.57 % while the primary phase corresponds to monoclinic Co_3Se_4 (space group *C 1 2/m 1*) with lattice parameters of $a = 12.26958 \pm 0.00071$ Å $b = 3.58218 \pm 0.00023$ Å
$c = 6.20174 \pm 0.00041$ Å.

To further characterize the electrochemical activity of these dissolved species, the soaked electrolyte was used to assemble a cell with an inert C Paper electrode and subjected to LSV. The results, presented in Fig. 7B are compared with the LSV of a pristine electrolyte. The data provide definitive evidence that the dissolved species detected by ICP-OES analysis are redox-active. An oxidation peak is observed at approximately 0.9 V, and the onset of a broader oxidation current begins around 1.7 V, confirming that the dissolved species undergo oxidation/reduction processes that could interfere with the cell's intended electrochemistry.

XRD analysis of CoSe electrodes after 200 cycles, unwashed, reveals extensive amorphization, as shown in Fig. 7C. Compared to the already degraded structure observed after soaking, the reflections are further diminished, indicating a progressive loss of crystallinity. This structural collapse is consistent with the conversion and dissolution mechanisms previously described and reinforces the role of amorphization in long-term degradation.

Raman spectroscopy of the CoSe electrode after 200 cycles, unwashed (Fig. 7D) demonstrates that the C-Se peak at 675 cm^{-1} and Co-Se bands at 468 and 507 cm^{-1} are still present, although with reduced intensity. This suggests that amorphized species remain in the electrode, likely contributing to the observed capacity. In contrast, when the CoSe electrode is soaked directly in the electrolyte, the characteristic Co-Se and C-Se vibrational bands disappear, suggesting that the electrolyte dissolves or alters these surface species (Fig. S7). This difference can be attributed to the lower electrolyte volume in the Swagelok configuration, which limits the extent of dissolution or washing away of the species during cycling.

Finally, to investigate the impact of cathode degradation on the Al anode, SEM-EDX analysis was conducted on foils retrieved after 20 cycles. Fig. 7E shows clear Co deposits on the Al foil after 20 cycles, providing direct evidence of Co migration from the cathode to the anode, accompanied by substantial degradation of the cathode (Fig. S8 and Fig S9). This Co deposition likely contributes to anode contamination, disrupting Al plating/stripping and accelerating capacity degradation. The improved performance observed in Cell 3, which used a fresh anode after activation, supports the hypothesis that anode contamination is a key factor in long-term degradation.

Based on the combined findings from electrochemical testing, *in operando* XRD, and *in situ/in operando* XAS, a comprehensive mechanism for charge storage and degradation in CoSe cathodes can now be proposed. The main charge storage process is proposed to involve a partially reversible phase transition, driven by the redox activity of Se. *In operando* SRD reveals a phase transition from hexagonal CoSe to cubic $CoSe_2$, while Se K-edge XAS confirms a reversible shift in the oxidation state of Se between Se^{2-} and a more oxidized form, $(Se_2)^{2-}$. The Co K-edge XAS shows no significant change in the oxidation state of Co, suggesting that Co remains electrochemically inactive and plays a structural role.

The suggested mechanism begins with an irreversible activation step, where the pristine CoSe irreversibly converts into an amorphous Co-Se matrix and crystalline $CoSe_2$ via a transient intermediate Co_3Se_4. This transformation is accompanied by the formation of soluble cobalt chloroaluminate species. Given the predominance of chloroaluminate species in the electrolyte, it is proposed that anions, likely $AlCl_4^-$ participate in the reaction as the balancing charge carriers, though direct in-situ confirmation of the anion's intercalation remains to be established.

$$6CoSe + 6AlCl_4^- \longrightarrow Co_3Se_4 + 3Co(AlCl_4)_{2(sln)} + (Se_2)^{2-} + 4e^- \quad (1)$$

The phase transition from Co_3Se_4 to $CoSe_2$ could happen through reintegration of $(Se_2)^{-2}$ (2) or further dissolution of $Co(AlCl_4)_2$ (3)

$$Co_3Se_4 + 2(Se_2)^{2-} \longrightarrow 3CoSe_2 + 2e^- \quad (2)$$

$$Co_3Se_4 + 2AlCl_4^- \longrightarrow 2CoSe_2 + Co(AlCl_4)_2 + 2e^- \quad (3)$$

The phase transition reaction can be simplified as:

$$6CoSe + 6AlCl_4^- \longrightarrow 3CoSe_2 + 3Co(AlCl_4)_2 + 6e^- \quad (4)$$

Or

$$6CoSe + 8AlCl_4^- \longrightarrow 2CoSe_2 + 4Co(AlCl_4)_2 + (Se_2)^{2-} + 6e^- \quad (5)$$

While the Se K-edge shifts approach the energy of elemental Se^0, the bonding environment differs, and the formation of Se^0 cannot be conclusively confirmed. The possibility of amorphous polyselenide species forming during charging remains open for future investigation.

Subsequently, the reversible capacity is proposed to arise from the reversible oxidation and reduction of Se within the amorphous CoSe

$$2Se^{2-} \rightleftharpoons (Se_2)^{2-} + 2e^- \quad (6)$$

While the redox activity of and the structural instability of the framework are experimentally supported, the specific stoichiometric coefficients and intermediate complexes represent a speculative model intended to illustrate the most probable reaction pathway within the chloroaluminate system.

The complex charge storage mechanism and degradation pathway is visually summarized in Fig. 8.

4. Conclusions

Carbon-encapsulated CoSe was synthesized via high-temperature selenization, as confirmed by Raman, XRD, and XAS, and evaluated as a cathode for RABs. *Electrochemical characterization* an initial phase transition and amorphization, which is essential for enabling reversible capacity but also initiates structural disorder and degradation and is accompanied by the dissolution of cobalt chloroaluminate species, proposedly $Co(AlCl_4)_2$, which migrates through the electrolyte and deposits on the Al anode. This degradation process causes loss of active material, alteration of the electrolyte composition and anode contamination, contributing to capacity fade. CA coupled with GCPL experiments demonstrated that replacing the electrolyte and Al foil after the initial degradation mitigates the effects of parasitic reactions and Co dissolution, leading to improved cycling stability.

In situ XRD and XAS studies show that CoSe undergoes a phase transition to $CoSe_2$ and Co_3Se_4, accompanied by structural disorder and a loss of long-range crystallinity. This transformation is only partially reversible, negatively impacting cycling stability. Se undergoes a redox transition from Se^{2-} to $(Se_2)^{2-}$ during charging and discharge. However, the structure of the discharged material deviates from the pristine state, indicating the modification of the Se framework upon cycling.

Ex situ characterization confirmed an initial dissolution of CoSe upon contact with the electrolyte and the electrochemical activity of the dissolved species. Furthermore, it was confirmed the amorphization of CoSe during cycling, but the amorphous species likely remain in the electrode as demonstrated by *ex situ* Raman results. SEM-EDX and electrochemical analyses confirmed Co dissolution and its migration to the Al anode, causing active material loss and degradation over cycling.

Finally, a new charge storage mechanism is proposed for the first time, based on dynamic characterization of CoSe. The primary charge storage process is proposed to be governed by an initial irreversible transformation from hexagonal CoSe to cubic $CoSe_2$ and amorphization of CoSe, within the amorphous lattice, Se is oxidized from Se^{2-} to $(Se_2)^{2-}$ during charge, and reduced back to Se^{2-}during discharge while Co remains electrochemically inactive. Importantly, the insights gained here are not limited to CoSe. They could be extrapolated to a broader class of transition metal chalcogenides and oxides, such as Co_9S_8, MoS_2, and V_2O_5, where similar dissolution phenomena have been linked to poor cyclability and capacity fading. Understanding the dissolution dynamics and redox behavior in chloride-rich electrolytes offers a valuable framework for designing more stable and reversible multivalent batteries.

Declaration of AI use

The authors declare the use of AI-based writing assistants, including Copilot, Gemini, and ChatGPT, to enhance the clarity and transparency of the text. All content generated with the assistance of these tools was carefully reviewed, edited, and verified by the authors, who assume full responsibility for the final content of the published article.

Funding sources

This work contributes to the research performed at CELEST (Center for Electrochemical Energy Storage Ulm-Karlsruhe) and was funded by the German Research Foundation (DFG) under Project ID 390874152 (POLiS Cluster of Excellence).

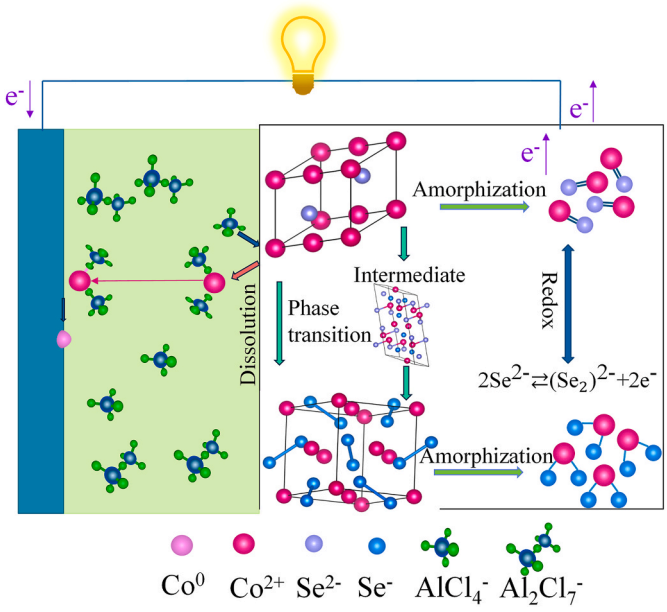

Fig. 8. Schematic of charge storage mechanism and degradation pathway of CoSe cathodes, scheme presented during cell charge.

CRediT authorship contribution statement

Eliana Fuentes-Mendoza: Conceptualization, Data curation, Formal analysis, Investigation, Methodology, Project administration, Software, Validation, Visualization, Writing – original draft, Writing – review & editing. **Angelina Sarapulova:** Conceptualization, Data curation, Supervision. **Ramon Zimmermanns:** Data curation, Formal analysis, Writing – review & editing. **Amirhossein Dorosti:** Investigation, Methodology, Writing – review & editing. **Volodymyr Baran:** Formal analysis, Validation, Writing – review & editing. **Fabian Jeschull:** Conceptualization, Data curation, Formal analysis, Funding acquisition, Investigation, Supervision, Validation, Writing – review & editing. **Sonia Dsoke:** Conceptualization, Data curation, Formal analysis, Funding acquisition, Supervision, Validation, Writing – review & editing.

Declaration of competing interest

The authors declare that they have no known competing financial interests or personal relationships that could have appeared to influence the work reported in this paper.

Acknowledgements

The authors acknowledge Dr. Nicholas Jobbitt's help in refining the language and in developing the scripts for the operando measurement plots. We acknowledge DESY (Hamburg, Germany), a member of the Helmholtz Association HGF, for the provision of experimental facilities. Parts of this research were carried out at PETRA III. Data was collected using (2) operated/provided by DESY Photon Science (or Helmholtz-Zentrum Hereon if applicable).

We would like to thank Dr. Edmund Welter for his assistance during the experiments. Beamtime was allocated for proposals I-20231008 and I-20231016.

Appendix A. Supplementary data

Supplementary data to this article can be found online at https://doi.org/10.1016/j.jpowsour.2026.240246.

Data availability

Data will be made available on request.

References

[1] International Energy Agency, Renewables 2023, 2024 www.iea.org.
[2] G. Gowrisankaran, S.S. Reynolds, M. Samano, Intermittency and the value of renewable energy, J. Polit. Econ. 124 (2016) 1187–1234, 0022-3808/2016/12404-0007.
[3] A.K. Barik, D.C. Das, A. Latif, S.M. Suhail Hussain, T.S. Ustun, Optimal voltage–frequency regulation in distributed sustainable energy-based hybrid microgrids with integrated resource planning, Energies 14 (2021), https://doi.org/10.3390/en14102735 (Basel).
[4] Y.S. Duh, K.H. Lin, C.S. Kao, Experimental investigation and visualization on thermal runaway of hard prismatic lithium-ion batteries used in smart phones, J. Therm. Anal. Calorim. 132 (2018) 1677–1692, https://doi.org/10.1007/s10973-018-7077-2.
[5] Y. Chen, Y. Kang, Y. Zhao, L. Wang, J. Liu, Y. Li, Z. Liang, X. He, X. Li, N. Tavajohi, B. Li, A review of lithium-ion battery safety concerns: the issues, strategies, and testing standards, J. Energy Chem. 59 (2021) 83–99, https://doi.org/10.1016/j.jechem.2020.10.017.
[6] B. Scrosati, History of lithium batteries, J. Solid State Electrochem. 15 (2011) 1623–1630, https://doi.org/10.1007/s10008-011-1386-8.
[7] J. Park, Z.-L. Xu, G. Yoon, S.K. Park, J. Wang, H. Hyun, H. Park, J. Lim, Y.-J. Ko, Y. S. Yun, K. Kang, Stable and high-power calcium-ion batteries enabled by calcium intercalation into graphite, Adv. Mater. 32 (2019) 1904411, https://doi.org/10.1002/adma.201904411.
[8] X. Li, Z. Chen, Y. Li, Y. Xu, D. Bai, B. Deng, W. Yao, J. Xu, Oxygen vacancy H2V3O8 nanowires as high-capacity cathode materials for aqueous zinc-ion batteries, Ionics 30 (2024) 5279–5289, 10.1007/s11581-024-05667-2.
[9] D. Muñoz-Torrero, J. Palma, R. Marcilla, E. Ventosa, A critical perspective on rechargeable Al-ion battery technology, Dalton Trans. 48 (2019) 9906–9911, 10.1039/c9dt02132a.
[10] C. Zor, S.J. Turrell, M.S. Uyanik, S. Afyon, Lithium plating and stripping: toward anode-free solid-state batteries, Adv. Energy Sustain. Res. 5 (2024) 2300001, 10.1002/aesr.202300001.
[11] E. Zemlyanushin, B. Schwarz, S. Dsoke, Dissolution of molybdenum current collector as crucial and undesired process in aluminum batteries, J. Power Sources 633 (2025) 236458 j.jpowsour.2025.236458.
[12] E. Zemlyanushin, A.L. Müller, T. Tsuda, S. Dsoke, Side-reactions of polyvinylidene fluoride and polyvinylidene chloride binders with aluminum chloride-based ionic liquid electrolyte in rechargeable aluminum-batteries, J. Electrochem. Soc. 171 (2024) 110507, https://doi.org/10.1149/1945-7111/ad8a93.
[13] E. Fuentes-Mendoza, M. Talari, E. Zemlyanushin, R. Cordoba, N. Sabi, S. Dsoke, Navigating the challenges of rechargeable aluminum battery research: material instabilities, technical hurdles, and future directions, Chemelectrochem 12 (2025) e202400705, https://doi.org/10.1002/celc.202400705.
[14] M. Talari, A. Sarapulova, E. Zemlyanushin, N. Sabi, A. Hofmann, V. Trouillet, S. Dsoke, Exploring the possibility of aluminum plating/stripping from a non-corrosive Al(OTf)3-based electrolyte, Batter. Supercaps 8 (2024), https://doi.org/10.1002/batt.202400317.
[15] S. Divya, T. Nann, High voltage carbon-based cathodes for non-aqueous aluminium-ion batteries, Chemelectrochem 8 (2020) 492–499, https://doi.org/10.1002/celc.202001490.
[16] M.-C. Huang, C.-H. Yang, C.-C. Chiang, S.-C. Chiu, Y.-F. Chen, C.-Y. Lin, L.-Y. Wang, Y.-L. Li, C.-C. Yang, W.-S. Chang, Influence of high loading on the performance of natural graphite-based Al secondary batteries, Energies 11 (2018) 2760, https://doi.org/10.3390/en11102760.
[17] X. Yu, B. Wang, D. Gong, Z. Xu, B. Lu, Graphene nanoribbons on highly porous 3D graphene for high-capacity and ultrastable Al-Ion batteries, Adv. Mater. 29 (2017) 1604118, https://doi.org/10.1002/adma.201604118.
[18] S. Wang, K.V. Kravchyk, F. Krumeich, M.V. Kovalenko, Kish graphite flakes as a cathode material for an aluminum chloride-graphite battery, ACS Appl. Mater. Interfaces 9 (2017) 28478–28485, https://doi.org/10.1021/acsami.7b07499.
[19] Q. Wang, D. Zheng, L. He, X. Ren, Cooperative effect in a graphite intercalation compound: enhanced mobility of AlCl4 in the graphite cathode of aluminum-ion batteries, Phys. Rev. Appl. 12 (2019) 044060, https://doi.org/10.1103/PhysRevApplied.12.044060.
[20] S. Wang, S. Jiao, W.L. Song, H. Sen Chen, J. Tu, D. Tian, H. Jiao, C. Fu, D.N. Fang, A novel dual-graphite aluminum-ion battery, Energy Storage Mater. 12 (2018) 119–127, https://doi.org/10.1016/j.ensm.2017.12.010.
[21] J. Qiao, H. Zhou, Z. Liu, H. Wen, J. Du, G. Wei, C. He, J. Yang, Dense integration of graphene paper positive electrode materials for aluminum-ion battery, Ionics 26 (2019) 245–254, https://doi.org/10.1007/s11581-019-03170-7.
[22] Z. Li, B. Niu, Y. Liu, J. Li, F. Kang, Prelithiation treatment of graphite as cathode material for rechargeable aluminum batteries, Electrochim. Acta 263 (2018) 68–75, https://doi.org/10.1016/j.electacta.2017.12.166.
[23] S. Chowdhury, N. Sabi, R.C. Rojano, N. Le Breton, A.K. Boudalis, S. Klayatskaya, S. Dsoke, M. Ruben, π-Conjugated metal free porphyrin as organic cathode for aluminum batteries, Batter. Supercaps 7 (2024) e202300285, https://doi.org/10.1002/batt.202300285.
[24] M. Walter, K.V. Kravchyk, C. Böfer, R. Widmer, M.V. Kovalenko, Polypyrenes as high-performance cathode materials for aluminum batteries, Adv. Mater. 30 (2018), https://doi.org/10.1002/adma.201705644.
[25] N.S. Hudak, Chloroaluminate-doped conducting polymers as positive electrodes in rechargeable aluminum batteries, J. Phys. Chem. C 118 (2014) 5203–5215, https://doi.org/10.1021/jp500593d.
[26] Q. Pang, J. Meng, S. Gupta, X. Hong, C.Y. Kwok, J. Zhao, Y. Jin, L. Xu, O. Karahan, Z. Wang, S. Toll, L. Mai, L.F. Nazar, M. Balasubramanian, B. Narayanan, D. R. Sadoway, Fast-charging aluminium-chalcogen batteries resistant to dendritic shorting, Nature 608 (2022) 704–711, https://doi.org/10.1038/s41586-022-04983-9.
[27] T. Abza, D.G. Dadi, F.G. Hone, T.C. Meharu, G. Tekle, E.B. Abebe, K.S. Ahmed, Characterization of cobalt sulfide thin films synthesized from acidic chemical baths, Adv. Mater. Sci. Eng. 2020 (2020), https://doi.org/10.1155/2020/2628706.
[28] S.B. Sibokoza, P.N. Mahlambi, S.B. Sibokoza, M.J. Moloto, N. Moloto, P.N. Sibiya, The effect of temperature and precursor concentration on the synthesis of cobalt sulphide nanoparticles using cobalt diethyldithiocarbamate complex, Chalcogenide Lett. 14 (2017) 69–78. https://chalcogen.ro/69_SibokozaSB.pdf.
[29] Z. Hu, K. Zhi, Q. Li, Z. Zhao, H. Liang, X. Liu, J. Huang, C. Zhang, H. Li, X. Guo, Two-dimensionally porous cobalt sulfide nanosheets as a high-performance cathode for aluminum-ion batteries, J. Power Sources 440 (2019), https://doi.org/10.1016/j.jpowsour.2019.227147.
[30] K. Liang, L. Ju, S. Koul, A. Kushima, Y. Yang, Self-supported tin sulfide porous films for flexible aluminum-ion batteries, Adv. Energy Mater. 9 (2019) 1802543, https://doi.org/10.1002/aenm.201802543.
[31] Z. Yu, Z. Kang, Z. Hu, J. Lu, Z. Zhou, S. Jiao, Hexagonal NiS nanobelts as advanced cathode materials for rechargeable Al-ion batteries, Chem. Commun. 52 (2016) 10427–10430, https://doi.org/10.1039/c6cc05974k.
[32] H. Li, H. Yang, Z. Sun, Y. Shi, H.M. Cheng, F. Li, A highly reversible Co3S4 microsphere cathode material for aluminum-ion batteries, Nano Energy 56 (2019) 100–108, https://doi.org/10.1016/j.nanoen.2018.11.045.
[33] T. Mori, Y. Orikasa, K. Nakanishi, C. Kezheng, M. Hattori, T. Ohta, Y. Uchimoto, Discharge/Charge reaction mechanisms of FeS2 cathode material for aluminum rechargeable batteries at 55°C, J. Power Sources 313 (2016) 9–14, https://doi.org/10.1016/j.jpowsour.2016.02.062.
[34] K. Zhang, Tae H. Lee, Joo H. Cha, Ho W. Jang, M. Shokouhimehr, J.-W. Choi, Properties of CoS 2/CNT as a cathode material of rechargeable aluminum-ion batteries, Electron. Mater. Lett. 15 (2019) 3, https://doi.org/10.1007/s13391-019-00169-0.
[35] B. Tan, T. Lu, W. Luo, Z. Chao, R. Dong, J. Fan, A novel MoS2-MXene composite cathode for aluminum-ion batteries, Energy Fuels 35 (2021) 12666–12670, https://doi.org/10.1021/acs.energyfuels.1c01461.
[36] X. Li, K. Li, S. Zhu, K. Fan, L. Lyu, H. Yao, Y. Li, J. Hu, H. Huang, Y. Mai, J. B. Goodenough, Fiber-in-Tube design of Co 9 S 8 -Carbon/Co 9 S 8 : enabling efficient sodium storage, Angew. Chem. 131 (2019) 6305–6309, https://doi.org/10.1002/ange.201900076.
[37] Z. Li, W. Lv, G. Wu, W. Zhang, Rhombic dodecahedron hetero-structure zn/co–se@C as cathode material for aluminum batteries with excellent electrochemical performance, J. Power Sources 511 (2021), https://doi.org/10.1016/j.jpowsour.2021.230455.
[38] Y. Du, B. Zhang, W. Zhang, H. Jin, J. Qin, J. Wan, J. Zhang, G. Chen, Interfacial engineering of Bi2Te3/Sb2Te3 heterojunction enables high–energy cathode for aluminum batteries, Energy Storage Mater. 38 (2021) 231–240, https://doi.org/10.1016/j.ensm.2021.03.012.
[39] Y. Chu, S. Xiong, Mixed transition-metal oxides@carbon core-shell nanostructures derived from heterometallic clusters for enhanced lithium storage, Chin. Chem. Lett. 33 (2022) 486–490, https://doi.org/10.1016/j.cclet.2021.06.074.
[40] X. Xu, X. Wang, S. Huo, X. Liu, X. Ma, M. Liu, J. Zou, Modulation of phase transition in cobalt selenide with simultaneous construction of heterojunctions for highly-efficient oxygen electrocatalysis in zinc–air battery, Adv. Mater. 36 (2024), https://doi.org/10.1002/adma.202306844.
[41] J.-L. Luo, X.-Y. Wang, R.-L. Liu, Y.-H. Zeng, H.-Q. Gu, L. Tan, X. Du, D. Li, J.-L. Luo, X.-Y. Wang, R.-L. Liu, Y.-H. Zeng, X. Du, D. Li, H.-Q. Gu, L. Tan, Cobalt selenide confined in nitrogen-doped carbon skeleton as high-rated capability anode for sodium-ion batteries, Rare Met. (2024) 6742–6750, https://doi.org/10.1007/s12598.
[42] T. Cai, L. Zhao, H. Hu, T. Li, X. Li, S. Guo, Y. Li, Q. Xue, W. Xing, Z. Yan, L. Wang, Stable CoSe2/carbon nanodice@reduced graphene oxide composites for high-performance rechargeable aluminum-ion batteries, Energy Environ. Sci. 11 (2018) 2341–2347, https://doi.org/10.1039/c8ee00822a.
[43] W. Xing, D. Du, T. Cai, X. Li, J. Zhou, Y. Chai, Q. Xue, Z. Yan, Carbon-encapsulated CoSe nanoparticles derived from metal-organic frameworks as advanced cathode material for Al-ion battery, J. Power Sources 401 (2018) 6–12, https://doi.org/10.1016/j.jpowsour.2018.08.079.
[44] L. Yao, S. Ju, X. Yu, Rational surface engineering of MXene@N-doped hollow carbon dual-confined cobalt sulfides/selenides for advanced aluminum batteries, J. Mater. Chem. A 9 (2021) 16878–16888, https://doi.org/10.1039/d1ta03465k.
[45] J. Qian, F. Sun, L. Qin, Hydrothermal synthesis of zeolitic imidazolate framework-67 (ZIF-67) nanocrystals, Mater. Lett. 82 (2012) 220–223, https://doi.org/10.1016/j.matlet.2012.05.077.

[46] A.C. Dippel, H.P. Liermann, J.T. Delitz, P. Walter, H. Schulte-Schrepping, O. H. Seeck, H. Franz, Beamline P02.1 at PETRA III for high-resolution and high-energy powder diffraction, J. Synchrotron Radiat. 22 (2015) 675–687, https://doi.org/10.1107/S1600577515002222.
[47] J. Filik, A.W. Ashton, P.C.Y. Chang, P.A. Chater, S.J. Day, M. Drakopoulos, M. W. Gerring, M.L. Hart, O.V. Magdysyuk, S. Michalik, A. Smith, C.C. Tang, N. J. Terrill, M.T. Wharmby, H. Wilhelm, Processing two-dimensional X-ray diffraction and small-angle scattering data in DAWN 2, J. Appl. Crystallogr. 50 (2017) 959–966, https://doi.org/10.1107/S1600576717004708.
[48] Z. Li, L.Y. Zhang, L. Zhang, J. Huang, H. Liu, ZIF-67-Derived CoSe/NC composites as anode materials for lithium-ion batteries, Nanoscale Res. Lett. 14 (2019), https://doi.org/10.1186/s11671-019-3194-5.
[49] Z.G. Pi, H. Ye, Z. Han, P. Yu, Z. Yin, X. Ma, Promising CoSe2-CNT composite catalyst for efficient photoelectrochemical hydrogen evolution reaction, Front. Mater. 9 (2022), https://doi.org/10.3389/fmats.2022.1005221.
[50] A.L. Ryser, D.G. Strawn, M.A. Marcus, J.L. Johnson-Maynard, M.E. Gunter, G. Möller, Micro-spectroscopic investigation of selenium-bearing minerals from the Western US phosphate resource area, Geochem. Trans. 6 (2005) 1–11, https://doi.org/10.1063/1.1852751.
[51] J.T. Olegario, N. Yee, M. Miller, J. Sczepaniak, B. Manning, Reduction of Se(VI) to se(-II) by zerovalent iron nanoparticle suspensions, J. Nanoparticle Res. 12 (2010) 2057–2068, https://doi.org/10.1007/s11051-009-9764-1.
[52] K. Jiang, B. Liu, M. Luo, S. Ning, M. Peng, Y. Zhao, Y.R. Lu, T.S. Chan, F.M.F. de Groot, Y. Tan, Single platinum atoms embedded in nanoporous cobalt selenide as electrocatalyst for accelerating hydrogen evolution reaction, Nat. Commun. 10 (2019), https://doi.org/10.1038/s41467-019-09765-y.
[53] S. Shen, Z. Wang, Z. Lin, K. Song, Q. Zhang, F. Meng, L. Gu, W. Zhong, Crystalline-amorphous interfaces coupling of CoSe2/CoP with optimized d-Band center and boosted electrocatalytic hydrogen evolution, Adv. Mater. 34 (2022), https://doi.org/10.1002/adma.202110631.
[54] F. Rahide, K. Palanisamy, J.K. Flowers, J. Hao, H.S. Stein, C. Kranz, H. Ehrenberg, S. Dsoke, Modification of Al surface via acidic treatment and its impact on plating and stripping, ChemSusChem 17 (2024), https://doi.org/10.1002/cssc.202301142.
[55] N. Sabi, K. Palanisamy, F. Rahide, S. Daboss, C. Kranz, S. Dsoke, Surface properties-performance relationship of aluminum foil as negative electrode for rechargeable aluminum batteries, Batter. Supercaps 6 (2023) e202300298, https://doi.org/10.1002/batt.202300298.
[56] W.A. Appiah, A. Stark, S. Lysgaard, J. Busk, P. Jankowski, J.H. Chang, A. Bhowmik, B. Gollas, J.M. Garcia-Lastra, Unveiling the plating-stripping mechanism in aluminum batteries with imidazolium-based electrolytes: a hierarchical model based on experiments and ab initio simulations, Chem. Eng. J. (Amsterdam, Neth.) 472 (2023), https://doi.org/10.1016/j.cej.2023.144995.
[57] K.V. Kravchyk, S. Wang, L. Piveteau, M.V. Kovalenko, Efficient aluminum chloride-natural graphite battery, Chem. Mater. 29 (2017) 4484–4492, https://doi.org/10.1021/acs.chemmater.7b01060.
[58] N. Canever, F.R. Hughson, T. Nann, Solid-electrolyte interphases (SEI) in nonaqueous aluminum-ion batteries, ACS Appl. Energy Mater. 3 (2020) 3673–3683, https://doi.org/10.1021/acsaem.0c00132.
[59] A.J. Bard, L.R. Faulkner, Electrochemical Methods : Fundamentals and Applications, second ed., 2001.
[60] H.A. oye, D.M. Gruen, Cobalt (II) species in fused chloride solvents 1173, Inorg. Chem. 4 (1965). https://pubs.acs.org/sharingguidelines.